JVST A
Journal of Vacuum Science & Technology A

ARTICLE

avs.scitation.org/journal/jva

Atomic layer deposition of aluminum oxyfluoride thin films with tunable stoichiometry

Cite as: J. Vac. Sci. Technol. A 38, 022407 (2020); doi: 10.1116/1.5135014
Submitted: 4 November 2019 · Accepted: 27 December 2019 ·
Published Online: 22 January 2020

Neha Mahuli, Andrew S. Cavanagh, and Steven M. George

AFFILIATIONS

Department of Chemistry, University of Colorado, Boulder, Colorado 80309-0215

Note: This paper is part of the 2020 Special Topic Collection on Atomic Layer Deposition (ALD).

ABSTRACT

Atomic layer deposition (ALD) of aluminum oxyfluoride (AlO_xF_y) thin films was demonstrated at 150 °C. Trimethyl aluminum, water, and HF were used as the aluminum, oxygen, and fluorine sources, respectively. *In situ* quartz crystal microbalance studies were utilized to monitor the AlO_xF_y deposition. Two deposition pathways were explored to grow the AlO_xF_y thin films based on the HF exchange method and the nanolaminate method. Linear AlO_xF_y growth was observed during both deposition methods. The HF exchange method is based on the thermodynamically favorable fluorination of Al_2O_3 by HF. Compositional control was achieved either by changing the HF pressure during the HF exposure or by varying the thickness of the underlying Al_2O_3 layer prior to the HF exposure. The nanolaminate method is based on the sequential deposition of Al_2O_3 ALD and AlF_3 ALD layers. The ratio of the number of Al_2O_3 ALD cycles to the number of AlF_3 ALD cycles is the main parameter used to control the O and F concentrations. *Ex situ* x-ray photoelectron spectroscopy (XPS) depth-profiling and Rutherford backscattering spectroscopy measurements were used to determine the composition of the AlO_xF_y thin films. The XPS depth-profile measurements confirmed the uniform distribution of Al, O, and F throughout the AlO_xF_y films using both deposition methods. Both techniques could obtain a wide range of compositional tunability between Al_2O_3 and AlF_3. Physical sputtering rates were also observed to be dependent on the relative concentrations of O and F in the AlO_xF_y films. The physical sputtering rates at 3 keV varied from 0.03 to 0.28 Å/s for Al_2O_3 and AlF_3, respectively.

I. INTRODUCTION

Plasma processing is used extensively in the semiconductor industry during device fabrication.[1,2] During plasma processing, various gases such as CF_4, C_2F_6, SF_6, Cl_2, NF_3, and O_2 are used to form halogen- and oxygen-containing plasmas.[3,4] These plasmas perform etching and oxidation reactions with the semiconductor wafers and also the vacuum chamber walls. The exposure of the chamber walls over time leads to erosion and particle formation. The changing chamber walls and particle formation subsequently affect the process uniformity and device reproducibility.[5–7] Protective coatings on the chamber walls are useful to minimize the damage resulting from plasma processing.[8,9]

Materials such as Al_2O_3 and Y_2O_3 are commonly explored as protective coatings because of their high corrosion resistance and chemical stability.[8,10–12] These oxide-based coatings are effective in oxygen-based plasma but provide less corrosion resistance under fluoride-based plasma environments.[12,13] Consequently, metal fluorides such as AlF_3 and YF_3 have been examined as alternative protective coatings. Metal fluoride coatings yield better stabilities in a fluoride-based plasma environment but are prone to higher erosion in oxygen-based plasmas.[13] Consequently, attention has been given to metal oxyfluorides as protective coating materials. Many studies have explored yttrium oxyfluoride (YO_xF_y) coatings in recent years.[8,9,11–15] Aluminum oxyfluoride (AlO_xF_y) may also yield corrosion resistance and chemical stability under different plasma environments.[16,17]

Various deposition techniques have been investigated to deposit metal oxyfluoride thin films such as sol-gel,[18] sputtering,[19–22] spray coating,[23] and metal-organic chemical vapor deposition.[24] Unfortunately, these techniques can produce nonconformal and nonuniform coatings. Atomic layer deposition (ALD) is a promising alternative technique to deposit highly conformal and pin-hole-free thin films even on high aspect ratio structures.[25–27] ALD is a variant of chemical vapor deposition and is based on two sequential, self-limiting surface chemical reactions.[27] ALD has been extensively explored for various binary compounds and has also been extended to ternary and quaternary materials.[27–29]

In this paper, the ALD of aluminum oxyfluorides is developed based on Al_2O_3 ALD and AlF_3 ALD. The ALD of aluminum-based binary compounds like Al_2O_3 and AlF_3 is well established. Al_2O_3 is most commonly performed with trimethyl aluminum (TMA) and water (H_2O) as the two precursors.[30–35] The chemical reactions during Al_2O_3 ALD can be written as follows:[33]

$$Al(OH)^* + Al(CH_3)_3(g) \rightarrow AlO_xAl(CH_3)_{3-x}^* + x\,CH_4(g), \quad (1)$$

$$AlO_xAl(CH_3)_{3-x}^* + (3-x)\,H_2O(g) \rightarrow AlO_xAl(OH)_{3-x} + (3-x)\,CH_4(g), \quad (2)$$

$$(2x-3)\,AlOH^* \leftrightarrow (x-1.5)\,AlOAl^* + (x-1.5)\,H_2O(g), \quad (3)$$

where the asterisks designate surface species. Self-limiting growth behavior is observed for Al_2O_3 ALD over a broad temperature window of 30–300 °C with a growth rate per cycle of ~1.1 Å/cycle at 150 °C.[32,35,36]

Similarly, AlF_3 ALD is also achieved by alternating exposures of TMA and HF in the temperature range of 75–200 °C with a growth rate of ~1.4 Å/cycle at 150 °C.[37] Other metal fluorides can also be deposited by ALD using HF as the fluorination reactant.[38] The reactions during AlF_3 ALD can be written as follows:[37]

$$AlF_3|xHF^* + Al(CH_3)_3(g) \rightarrow AlF_3|AlF_x(CH_3)_{3-x}^* + x\,CH_4(g), \quad (4)$$

$$AlF_3|AlF_x(CH_3)_{3-x}^* + 3\,HF(g) \rightarrow AlF_3|AlF_3|xHF^* + (3-x)\,CH_4(g). \quad (5)$$

In Eq. (4), HF is adsorbed on the AlF_3 surface and reacts with TMA to produce $AlF_x(CH_3)_{3-x}$ species. The $AlF_x(CH_3)_{3-x}$ species then react with HF to produce AlF_3 as given in Eq. (5).

Two distinct deposition pathways were utilized for AlO_xF_y ALD based on the HF exchange method and the nanolaminate method. *In situ* quartz crystal microbalance (QCM) studies were conducted to understand the growth mechanism during both deposition pathways. Compositional tunability was verified using *ex situ* x-ray photoelectron spectroscopy (XPS) and Rutherford backscattering spectroscopy (RBS) analysis. In addition, the physical sputtering rates of the AlO_xF_y films were determined while performing the *ex situ* XPS depth-profile analysis.

II. EXPERIMENT

A. Viscous flow reactor with *in situ* QCM

Atomic layer deposition of the AlO_xF_y thin films was performed at 150 °C in a custom-built hot wall viscous flow reactor.[36] Trimethyl aluminum (TMA, 97%, Sigma Aldrich) was used as the aluminum source. Water (HPLC grade H_2O, Sigma Aldrich) and HF-pyridine (70% wt. HF, Sigma Aldrich) were used as oxygen and fluorine sources, respectively. All the precursors were used as-received without any further purification and were maintained at room temperature. HF-pyridine was stored in a gold-coated stainless steel container.

High purity argon gas (Airgas, prepurified) was used as the purge gas. The reactor pressure was maintained at 1 Torr at all times using a continuous flow of Ar gas at 200 sccm controlled by mass flow controllers (Type 1179A, MKS). Pressure changes in the reactor were monitored using a bakeable capacitance manometer (Baratron 121A, MKS). A proportional-integral-derivative temperature controller (2604, Eurotherm) was used to maintain the reactor temperature at ±0.04 °C from the set point at 150 °C.

A mechanical rotary vane pump (Pascal 2010SD, Pfeiffer Vacuum) was used to achieve the desired vacuum conditions during AlO_xF_y ALD. An activated alumina trap (Visi-trap, LACO Technologies) was used at the inlet of the vacuum pump to remove excessive unreacted precursors. The exhaust stream of the pump was also fed through a calcium oxide solution to remove further any remaining unreacted HF precursor.

An *in situ* quartz crystal microbalance (QCM) was utilized to examine the reactions during AlO_xF_y ALD at 150 °C.[36] The QCM sensor used in this study was a gold-coated, polished AT cut quartz crystal (Colorado Crystal Corp.) with a resonant frequency at 6 MHz. The QCM sensor was held in a commercially available bakeable crystal drawer and retainer assembly (BSH-150, Inficon) and sealed using a high temperature epoxy (Epo-Tek H21D, Epoxy Technology). An additional Ar flow of 20 sccm was maintained through the QCM housing to avoid any deposition on the backside of the crystal.[36] This additional Ar flow increased the reactor pressure by 0.1 Torr.

The real-time frequency fluctuations of the QCM were recorded using a QCM monitor (Maxtek TM-400, Inficon). The Saurbrey equation was used to convert the frequency changes to mass changes. The bare quartz crystal was first coated with 250 cycles of Al_2O_3 ALD before any AlO_xF_y ALD experiment. One hundred cycles of Al_2O_3 ALD were also deposited between consecutive experiments to define the same starting surface.

B. *Ex situ* compositional analysis using XPS and RBS

Si (111) coupons with dimensions of 1×1 in.^{2} were used as substrates for all the *ex situ* measurements. Depth-profile XPS measurements (PHI 5600, RBD Instruments) were conducted with a monochromatic Al-Kα (1486.6 eV) x-ray source to study the elemental composition of the AlO_xF_y thin films. Depth-profiling was achieved with Ar ion sputtering at an energy of 3 keV. The AugerScan software package (AugerScan, RBD Instruments) was utilized to collect all the XPS data. The CasaXPS software package (CasaXPS, Casa Software) was used to analyze the XPS data.

RBS measurements were performed at the Laboratory for Surface Modification at Rutgers University. The RBS measurements determined the precise composition of the various AlO_xF_y thin films. The experimental RBS setup consisted of an He^{++} beam at 2 MeV oriented normal to the substrate surface. The detector was placed at a scattering angle of 163°, and the energy resolution was 20 keV. SIMNRA software was used to fit all the elements in the RBS spectra.

C. AlO_xF_y growth methods

AlO_xF_y ALD was performed using two different methods. These methods were the HF exchange method and the

nanolaminate method shown in Figs. 1(a) and 1(b), respectively. AlO_xF_y deposition using the HF exchange method displayed in Fig. 1(a) is primarily based on HF fluorination of Al_2O_3. This process involves depositing "n" cycles of Al_2O_3 ALD followed by the HF fluorination reaction. The combination of these two steps comprises one supercycle denoted by the ratio "n:m," where "n" is the number of Al_2O_3 ALD cycles and "m" is the number of HF doses.

According to thermodynamics, HF fluorination of Al_2O_3 to produce AlF_3 as given by Eq. (6) is a spontaneous reaction with a standard Gibb's free energy of $\Delta G° = -63$ kcal/mol at 150 °C.[39]

$$Al_2O_3 + 6HF(g) \rightarrow 2AlF_3 + 3H_2O(g). \quad (6)$$

The resulting reaction product, AlF_3, is stable and nonvolatile at the deposition temperature. Stoichiometry in the AlO_xF_y films can be controlled by controlling fluorination of the underlying Al_2O_3 layer.

AlO_xF_y was also deposited using the nanolaminate method displayed in Fig. 1(b). Nanolaminate thin films were produced by alternating deposition of "n" cycles of Al_2O_3 ALD followed by "m" cycles of AlF_3 ALD at 150 °C. The combination of "n" cycles of Al_2O_3 ALD and "m" cycles of AlF_3 ALD defines one supercycle. The oxygen and fluorine concentrations in these films were controlled by varying the "n:m" ratio.

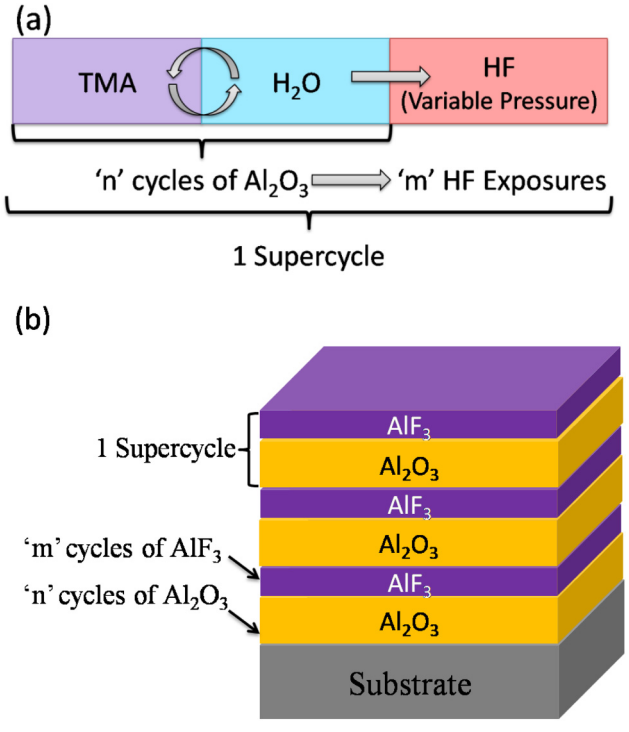

FIG. 1. Schematic of AlO_xF_y ALD using (a) the HF exchange method and (b) the nanolaminate method.

III. RESULTS AND DISCUSSION

Figure 2(a) shows the mass gain recorded by the *in situ* QCM during 25 supercycles of AlO_xF_y deposition using the HF exchange method at 150 °C. One supercycle consisted of one cycle of Al_2O_3 ALD followed by a single HF exposure. One AlO_xF_y ALD cycle was defined by a 0.5 s dose of TMA, 45 s of Ar purge, a 0.3 s dose of H_2O, 45 s of Ar purge, a 0.5 s HF dose, and 45 s of Ar purge. This dosing sequence is designated as (0.5-45-0.3-45-0.5-45). A long purge time of 45 s was used between each precursor exposure to ensure complete removal of excess precursor molecules and by-products. Precursor pressures were maintained at 45, 50, and

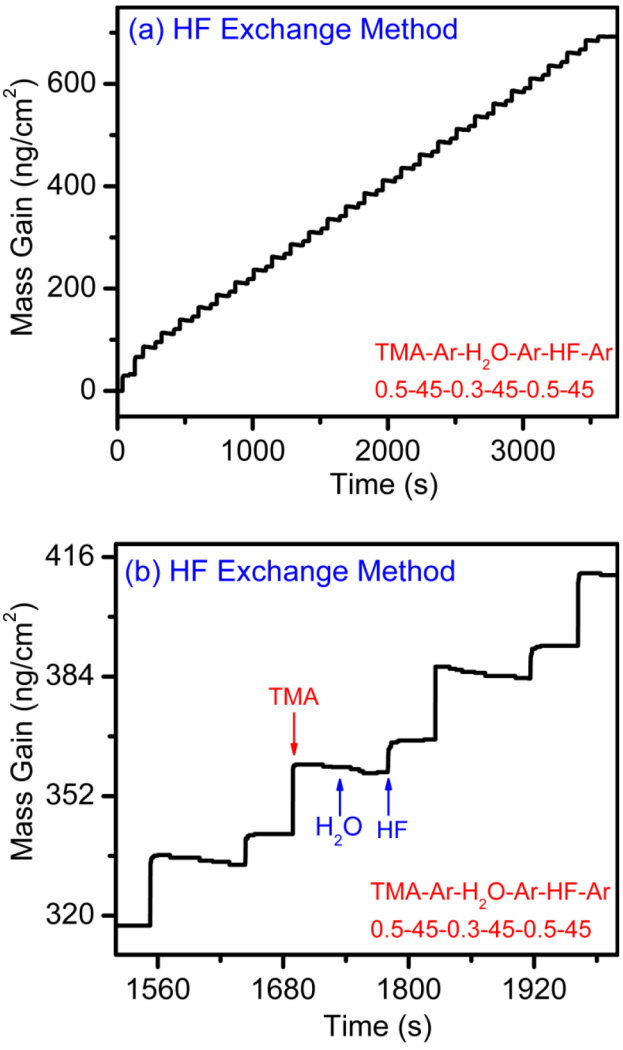

FIG. 2. (a) Mass gain vs time recorded by the QCM during 25 consecutive AlO_xF_y supercycles using the HF exchange method at 150 °C with a dosing sequence of (0.5-45-0.3-45-0.5-45). (b) Expansion of mass gain vs time for three AlO_xF_y supercycles from the linear growth regime in Fig. 2(a).

20–25 mTorr above base pressure for TMA, H_2O, and HF, respectively, unless stated otherwise. Figure 2(a) shows a linear mass gain versus time during AlO_xF_y deposition. The mass gain per cycle (MGPC) during these 25 supercycles was $\Delta m = 24–25$ ng/(cm^2 cycle).

Figure 2(b) shows an expansion of the mass gain during three consecutive AlO_xF_y supercycles in the linear growth regime of Fig. 2(a). A mass gain after TMA exposure of $\Delta m_{TMA} = 18–19$ ng/cm^2 and a mass loss after H_2O exposure of $\Delta m_{H2O} = -2$ ng/cm^2 were observed during the supercycle. When HF was introduced following the TMA and H_2O exposures, a mass gain of $\Delta m_{HF} = 8–9$ ng/cm^2 was observed during the fluorination reaction. The overall mass gain per cycle during AlO_xF_y ALD was $\Delta m = \Delta m_{TMA} + \Delta m_{H2O} + \Delta m_{HF} = 24–25$ ng/(cm^2 cycle).

Figure 3 displays the *ex situ* XPS depth-profile analysis of the AlO_xF_y thin film with a thickness of 30 nm grown by the HF exchange method on Si(111) at 150 °C using the dosing sequence of (0.5-45-0.3-45-0.5-45). The XPS depth-profile shows a continuous and uniform distribution of Al, O, and F throughout the film. Adventitious carbon was observed on the surface prior to any sputtering. The film composition was $AlO_{0.2}F_2$ based on the bulk atomic concentrations. However, preferential sputtering of fluorine has been observed earlier during the depth-profiling of AlF_3 thin films.[37,40] To avoid the problems caused by preferential sputtering, Rutherford backscattering spectroscopy (RBS) was also used to determine the composition of the AlO_xF_y thin films.

Figure 4 shows the RBS spectrum of an AlO_xF_y thin film with a thickness of 30 nm grown using the HF exchange method on Si(111) at 150 °C using the dosing sequence of (0.5-45-0.3-45-0.5-45). The RBS spectrum shows three distinct peaks over the energy range of 200–1200 keV. The peak corresponding to an energy of 1100 keV was assigned to Al. The peaks at energies of 725 and 850 keV were assigned to O and F, respectively. Based on the RBS analysis, the composition of this film was $AlO_{0.5}F_{1.8}$. Carbon is beyond the detection limit of this RBS spectrum.

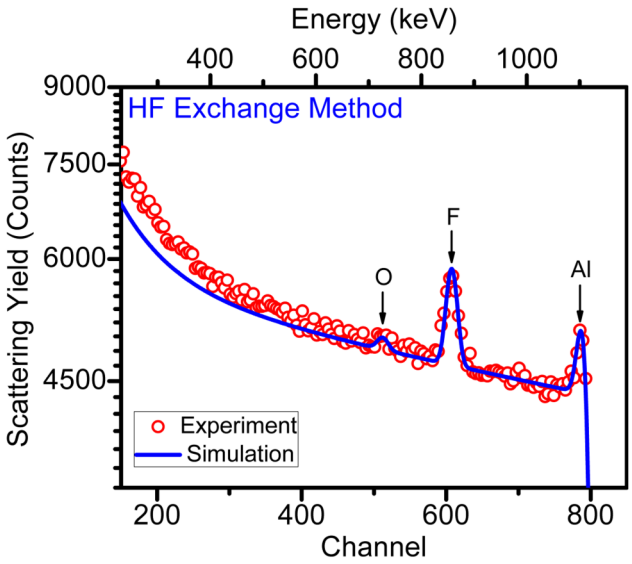

FIG. 4. Rutherford backscattering spectrum (RBS) of AlO_xF_y thin films with a thickness of 30 nm grown by the HF exchange method on the Si(111) substrate at 150 °C with a dosing sequence of (0.5-45-0.3-45-0.5-45).

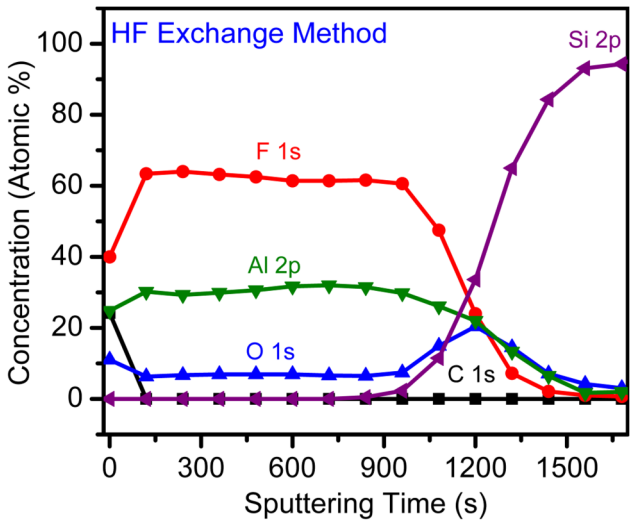

FIG. 3. Compositional depth profile of AlO_xF_y thin films with a thickness of 30 nm grown by the HF exchange method on the Si(111) substrate at 150 °C with a dosing sequence of (0.5-45-0.3-45-0.5-45) measured by x-ray photoelectron spectroscopy (XPS).

Other AlO_xF_y compositions can be obtained by varying the number of Al_2O_3 ALD cycles prior to the HF exposure or changing the HF pressure during the HF exposure. Figure 5 shows mass gain recorded during four consecutive AlO_xF_y supercycles at 150 °C,

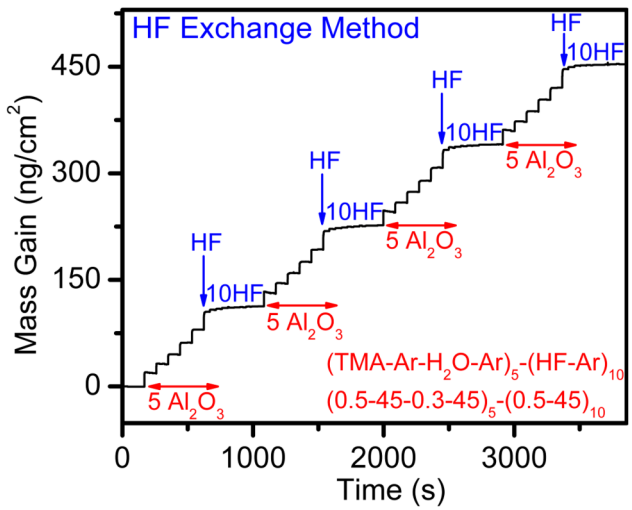

FIG. 5. Mass gain vs time recorded by QCM during four consecutive AlO_xF_y supercycles grown by the HF exchange method at 150 °C using a dosing sequence of $(0.5\text{-}45\text{-}0.3\text{-}45)_5$–$(0.5\text{-}45)_{10}$.

where each supercycle consisted of five cycles of Al_2O_3 ALD followed by ten HF exposures. An overall mass gain of $\Delta m_{Al2O3} = 75–78\ ng/cm^2$ was measured after five cycles of Al_2O_3 ALD. A mass gain of $\Delta m_{HF} = 29–30\ ng/cm^2$ was then observed after ten consecutive HF exposures. The mass gain per supercycle was $\Delta m = \Delta m_{Al2O3} + \Delta m_{HF} = 100–102\ ng/(cm^2\ cycle)$. The dosing sequence was $(0.5\text{-}45\text{-}0.3\text{-}45)_n - (0.5\text{-}45)_m$, where $n = 5$ represents five cycles of Al_2O_3 ALD and $m = 10$ designates the ten HF exposures. The mass gain during the fluorination step of $\Delta m_{HF} = 29–30\ ng/cm^2$ is attributed to the following reaction:[41]

$$Al_2O_3 + zHF(g) \rightarrow 2AlO_{(6-z)/4}F_{z/2} + (z/2)\,H_2O(g). \quad (7)$$

In addition to varying the number of Al_2O_3 ALD cycles, the AlO_xF_y film composition can be controlled by varying the pressure during the HF exposure. Figure 6(a) shows mass changes recorded during the fluorination step utilizing ten consecutive HF doses where the HF pressure was varied from 20 to 200 mTorr while keeping the dose time constant at 0.5 s. There is a progressive increase in Δm_{HF} with HF pressure. Δm_{HF} increases from 29–30 to 38–39 ng/cm^2 when the HF pressure is raised from 20 to 200 mTorr. Similar increases in fluorination of Al_2O_3 with HF pressure were observed in earlier studies of Al_2O_3 atomic layer etching using HF and trimethylaluminum (TMA).[41] Figure 6(a) also indicates that the mass gain reaches a saturation level during ten consecutive HF doses. This saturation behavior suggests that HF exchange and F diffusion into the Al_2O_3 ALD film reaches a limit at each HF pressure.

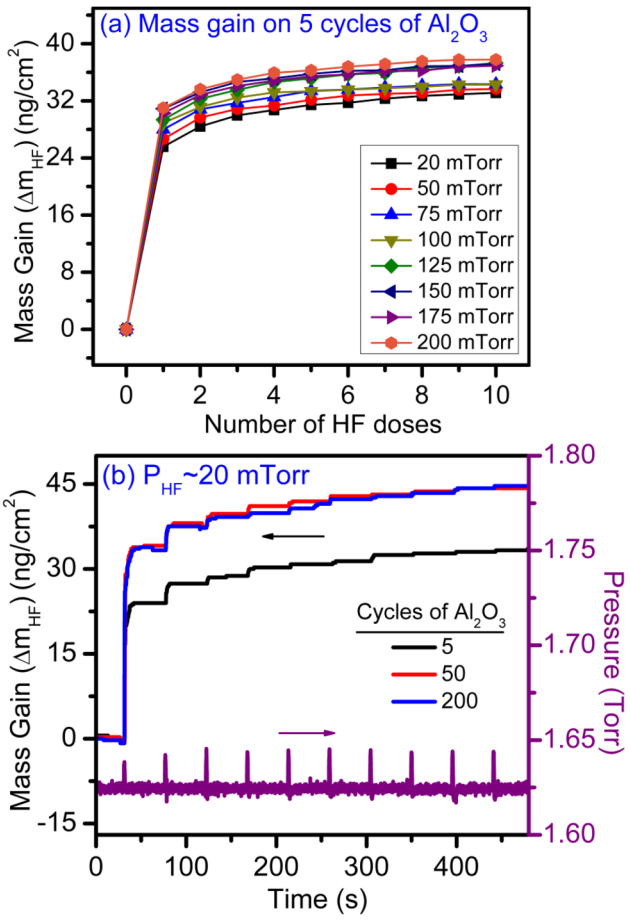

FIG. 6. (a) Effect of HF pressure on mass gain (Δm_{HF}) vs number of HF doses on five cycles of Al_2O_3 ALD at 150 °C. (b) Effect of underlying Al_2O_3 thickness determined by the number of cycles of Al_2O_3 ALD on mass gain (Δm_{HF}) vs time during 10 HF doses at 20 mTorr.

The penetration depth of F into the Al_2O_3 ALD film is another factor for the incorporation of F into Al_2O_3. Figure 6(b) shows the effect of the underlying Al_2O_3 thickness on the fluorination reaction while keeping the HF pressure constant at 20 mTorr. The mass gains during these HF doses were measured for three different Al_2O_3 thicknesses. These Al_2O_3 thicknesses were defined by 5 cycles, 50 cycles, and 200 cycles of Al_2O_3 ALD. The mass gains were 29–30 ng/cm^2 for 5 cycles of Al_2O_3 ALD and 44–45 ng/cm^2 for 50 cycles and 200 cycles of Al_2O_3 ALD. These results confirm that the fluorination reaction is not limited to the surface. The increase in Δm_{HF} with Al_2O_3 film thickness indicates that fluorination occurs in the bulk of the Al_2O_3 ALD film. The constancy in mass gain for fluorination of Al_2O_3 ALD films deposited using 50 and 200 Al_2O_3 ALD cycles suggests that the fluorination depth is limited to less than or equal to the Al_2O_3 film thickness corresponding to 50 cycles of Al_2O_3 ALD.

An approximate fluorination depth into Al_2O_3 can also be estimated based on the QCM mass gain of 45 ng/cm^2 observed in Fig. 6(b). Based on the fluorination reaction for Al_2O_3 by HF given in Eq. (6), the molar mass change for the fluorination reaction is 66.0 g/mol. The mass gain of 45 ng/cm^2 is consistent with 6.82×10^{-10} mol/cm^2 of Al_2O_3 converted to $2AlF_3$. This conversion of Al_2O_3 to $2AlF_3$ will produce 1.36×10^{-9} mol/cm^2 of AlF_3. The mass of this AlF_3 layer is 1.15×10^{-7} g/cm^2. This AlF_3 layer has a thickness of 4.0×10^{-8} cm or 4.0 Å given an AlF_3 density of 2.88 g/cm^3. This estimated AlF_3 layer thickness is very close to the AlF_xO_y film thicknesses determined by XPS analysis following HF exposures on Al_2O_3 in recent studies.[41]

Additional experiments can be performed to demonstrate that F can diffuse into the Al_2O_3 film. Although the results in Fig. 6 suggest that the fluorination reaches saturation in the Al_2O_3 ALD film, diffusion can extend fluorination of the Al_2O_3 ALD film. Figure 7 shows the mass gain during HF exposures after different aging times at 150 °C. After the aging times of 30 min, 1 h, 2 h, and 3.5 h, F diffuses deeper into the Al_2O_3 ALD film. This diffusion allows more HF to absorb into the Al_2O_3 ALD film and leads to larger Δm_{HF} values.

The composition of AlO_xF_y films can be controlled using the HF exchange method by varying the thickness of the underlying Al_2O_3 layer and the HF pressure. Figure 8(a) shows the AlO_xF_y compositional tunability represented by the F/Al ratio with respect to the deposition parameters. The relative composition of Al, O, and F in these films is obtained by RBS analysis. Precise control in the fluorine concentration in the films can be obtained from Al_2O_3 to AlF_3. Table I also reports the film composition from both RBS

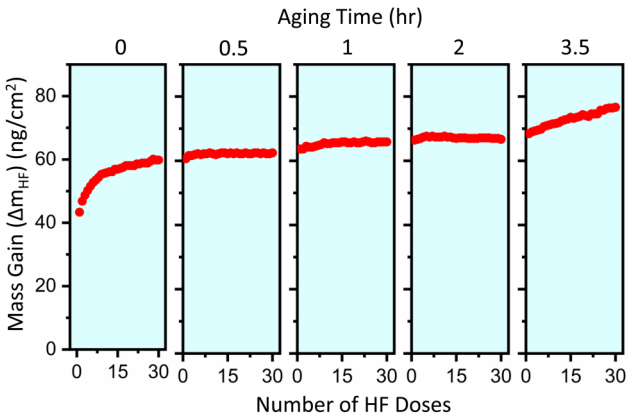

FIG. 7. Effect of aging time on mass gain (Δm_{HF}) during 30 HF doses on Al_2O_3 at 150 °C. Aging times are increased sequentially before the next set of 30 HF doses.

and XPS analysis. Depth-profile XPS analysis measures reduced F concentrations in the films relative to the RBS measurements. These lower fluorine concentrations are attributed to preferential F sputtering.

The nanolaminate method can also be used to control the AlO_xF_y film composition. Figure 9(a) shows the mass gain recorded by the *in situ* QCM analysis during ten consecutive supercycles of AlO_xF_y grown using the nanolaminate method at 150 °C. For these results, the reaction sequence for one AlO_xF_y supercycle was five cycles of Al_2O_3 ALD followed by one cycle of AlF_3 ALD. The dosing sequence for this 5:1 supercycle was $(0.5\text{-}45\text{-}0.3\text{-}45)_5$–$(0.5\text{-}45\text{-}0.5\text{-}45)_1$. The precursor pressures were 45, 50, and 20–25 mTorr above base pressure for TMA, H_2O, and HF, respectively. Linear growth was measured by the mass gain versus time throughout ten supercycles of AlO_xF_y growth. The overall mass gain per supercycle during 5:1 AlO_xF_y growth was 123–125 ng/(cm^2 cycle).

Figure 9(b) shows an expansion of the mass gain during two consecutive AlO_xF_y supercycles in the linear growth regime of Fig. 9(a). The five cycles of Al_2O_3 ALD produce a mass gain of $\Delta m_{Al2O3} = 75$–78 ng/cm^2. In addition, the TMA and HF exposures after the five Al_2O_3 ALD cycles produce a mass gain of $\Delta m_{AlF3} = 48$–50 ng/cm^2. There is a large mass gain during HF exposure in the AlF_3 cycle. This mass gain results from the surface reaction with Al-CH_3* surface species and the HF exchange reaction with the underlying Al_2O_3 layer. The total mass gain during the 5:1 supercycle was $\Delta m = \Delta m_{Al2O3} + \Delta m_{AlF3} = 123$–$125$ ng/(cm^2 cycle).

The growth of nanolaminates requires the nucleation of AlF_3 ALD on Al_2O_3 and Al_2O_3 ALD on AlF_3. Nucleation of both AlF_3 ALD on Al_2O_3 and Al_2O_3 ALD on AlF_3 was further studied as shown in Fig. 10. Figure 10(a) shows the mass gain versus time during the first six cycles of AlF_3 ALD on an Al_2O_3 ALD film that was terminated with Al-OH* after the last H_2O exposure. The first few AlF_3 ALD cycles display mass gains that are substantially higher than the mass gains during AlF_3 ALD steady-state growth. During the first AlF_3 ALD cycle, mass gains of 30.1 and 40.4 ng/cm^2 were obtained during the TMA and HF exposures, respectively.

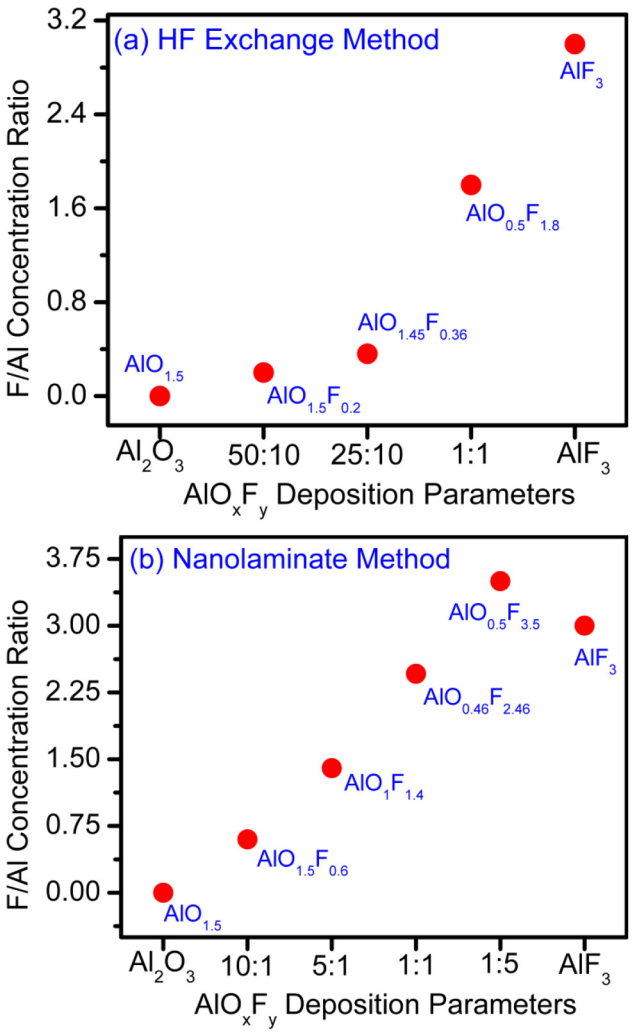

FIG. 8. Compositional tunability as measured by the F/Al concentration ratio from the RBS analysis for various deposition parameters for (a) the HF exchange method and (b) the nanolaminate method.

The high mass gain during the first HF exposure of $\Delta m_{HF} = 40.4$ ng/cm^2 is a combination of the HF reaction with Al-CH_3* species and the exchange of F with O and F diffusion into the underlying Al_2O_3 film. The subsequent HF exposures during AlF_3 ALD on Al_2O_3 display substantially lower mass gains. The second HF exposure has a mass gain of 11.4 ng/cm^2. The third HF exposure displays a mass gain of 6.8 ng/cm^2. After the third AlF_3 ALD cycle, the AlF_3 ALD is in the steady-state AlF_3 ALD growth regime.

Figure 10(b) shows the mass gain versus time during the first six cycles of Al_2O_3 ALD on an AlF_3 ALD film that was terminated with Al-F* after the last HF exposure. The first Al_2O_3 ALD cycle displays mass gains of 16.9 and −1.4 ng/cm^2 for the TMA and H_2O exposures, respectively. The slight mass loss during the first H_2O exposure can be justified as a combination of H_2O reacting with

TABLE I. Summary of compositional analysis by depth-profile XPS and RBS along with respective rates of sputtering for various AlO_xF_y samples grown by HF exchange and nanolaminate methods at 150 °C.

Deposition condition	Composition		Rate of sputtering (Å/s)
	XPS	RBS	
Al_2O_3	$AlO_{1.13}F_0$	$AlO_{1.5}F_0$	0.03
AlF_3	$AlO_{0.15}F_{1.8}$	AlO_0F_3	0.28
HF exchange method			
50:10	$AlO_{1.1}F_{0.04}$	$AlO_{1.5}F_{0.2}$	0.04
25:10	$AlO_1F_{0.1}$	$AlO_{1.45}F_{0.36}$	0.12
1:1	$AlO_{0.2}F_2$	$AlO_{0.5}F_{1.8}$	0.23
Nanolaminate method			
10:1	$AlO_{1.1}F_{0.2}$	$AlO_{1.5}F_{0.6}$	0.05
5:1	$AlO_{0.8}F_{0.8}$	$AlO_{1.0}F_{1.4}$	0.14
1:1	$AlO_{0.2}F_{1.8}$	$AlO_{0.46}F_{2.46}$	0.25
1:5	$AlO_{0.12}F_{1.9}$	$AlO_{0.3}F_{3.5}$	0.27

Al-CH_3* surface species and O exchange with F in the underlying AlF_3 layer. This exchange reaction can be described by

$$2AlF_3 + 3H_2O(g) \rightarrow Al_2O_3 + 6HF(g). \quad (8)$$

This conversion reaction is not predicted to be thermochemically favorable because the standard Gibbs free energy is $\Delta G° = +63$ kcal at 150 °C.[39] However, the conditions during H_2O exposure to the AlF_3 surface terminated with Al-CH_3* surface species are far from the standard state. The Al_2O_3 growth after the initial Al_2O_3 ALD cycles quickly approaches the steady-state reactions that have been observed earlier.[33]

Figure 11 displays the depth-profile XPS analysis of an AlO_xF_y thin film with a thickness of 30 nm grown by the 5:1 nanolaminate method on Si(111) at 150 °C using a dosing sequence given by $(0.5\text{-}45\text{-}0.3\text{-}45)_5$–$(0.5\text{-}45\text{-}0.5\text{-}45)_1$. A continuous and uniform distribution of Al, O, and F is measured throughout the film thickness. The film composition was $AlO_{0.8}F_{0.8}$ based on bulk atomic concentrations. However, lower fluorine signals in the bulk of AlO_xF_y are expected when measured by XPS due to preferential sputtering of fluorine.[37,40] RBS was utilized as an alternative elemental analysis technique to determine the exact composition of the AlO_xF_y thin films.

Figure 12 displays the RBS analysis in the energy range of 200–1200 keV for an AlO_xF_y thin film with a thickness of 30 nm grown by the nanolaminate method on Si(111) at 150 °C. This film was also grown using the 5:1 nanolaminate method. The RBS spectrum shows three peaks at energies of 1100, 725, and 850 keV corresponding to Al, O, and F, respectively. These RBS results are consistent with a film composition of $AlO_1F_{1.4}$.

Table I summarizes the compositions of AlO_xF_y thin films grown by the nanolaminate method. Various compositions are achieved by employing "n" cycles of Al_2O_3 ALD followed by "m" cycles of AlF_3 ALD at 150 °C. Figure 8(b) shows the AlO_xF_y compositional tunability represented by the F/Al ratio with respect to various deposition parameters. A wide range of oxygen to fluorine ratios was achieved based on the deposition parameters over the entire composition range from Al_2O_3 to AlF_3. The composition of the 1:5 AlO_xF_y sample was determined to be $AlO_{0.5}F_{3.5}$ from RBS analysis. The excessive fluorine may result from more F residing at the interface between the AlF_3 layer and the O layer formed using only one Al_2O_3 ALD cycle.

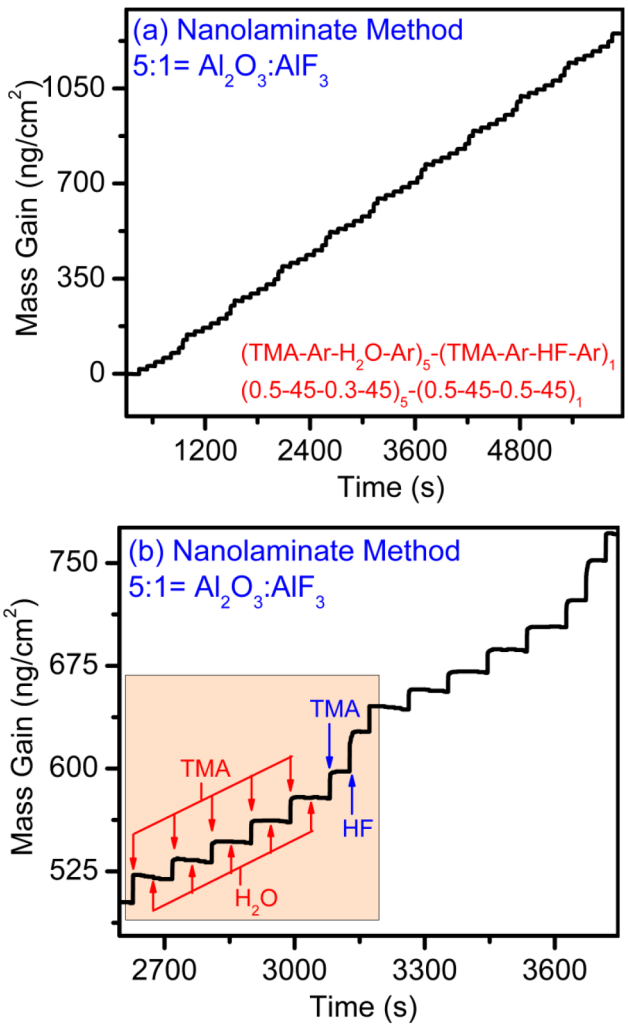

FIG. 9. (a) Mass gain vs time recorded by the QCM during ten consecutive AlO_xF_y supercycles using the nanolaminate method at 150 °C with a dosing sequence of $(0.5\text{-}45\text{-}0.3\text{-}45)_5$–$(0.5\text{-}45\text{-}0.5\text{-}45)_1$. (b) Expansion of mass gain vs time from (a) for two AlO_xF_y supercycles.

The physical sputtering rate of the AlO_xF_y thin films was also measured during the XPS depth-profile analysis. The sputtering rate was determined using the following equation:

$$\text{Physical sputtering rate} = \frac{\text{Thickness of } AlO_xF_y \text{ film}}{\text{Sputtering time}}. \quad (9)$$

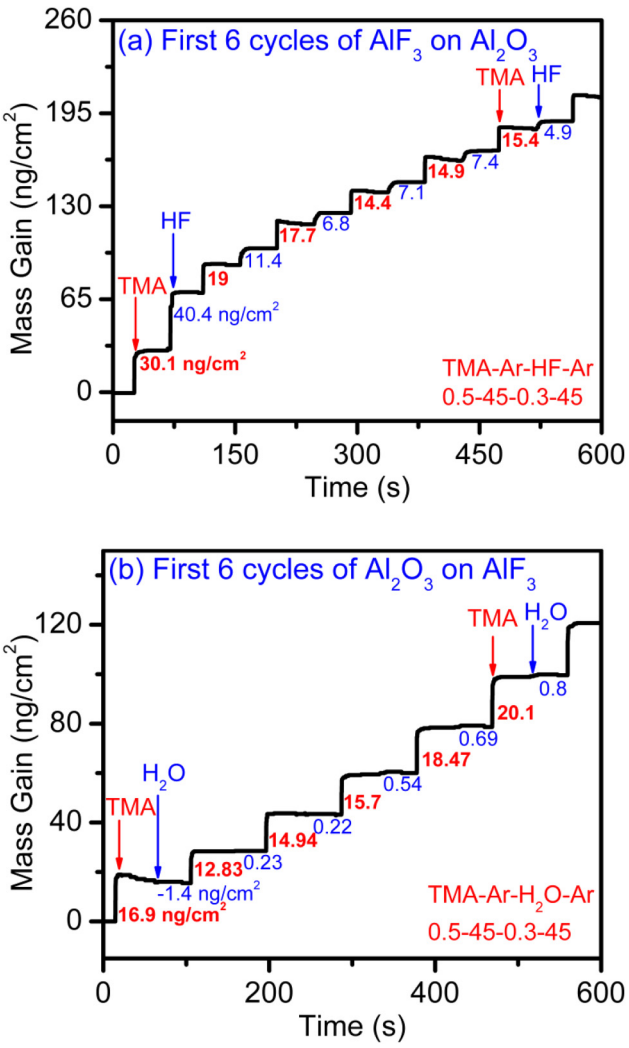

FIG. 10. Mass gain vs time recorded by the QCM during the first six ALD cycles at 150 °C for (a) AlF_3 ALD on the Al-OH* terminated Al_2O_3 surface and (b) Al_2O_3 ALD on the Al-F* terminated AlF_3 surface.

The thickness of all the AlO_xF_y films was kept constant at 30 nm, as measured by XRR measurements. The sputtering time was the time required to reach the substrate surface, which was when the XPS intensity of Si 2p reached 50 at. %.[42,43] The physical sputtering rates were measured between 0.03 and 0.28 Å/s for Al_2O_3 and AlF_3, respectively. The sputtering rate of AlF_3 is much higher than the sputtering rate of Al_2O_3 as reported earlier.[42]

Figure 13(a) displays the sputtering rates versus the F/Al ratio for various AlO_xF_y thin films grown by the HF exchange method. Figure 13(b) shows the sputtering rates versus the F/Al ratio for various AlO_xF_y thin films grown by the nanolaminate method. Exact compositions of all the samples from RBS analysis are also given next to the sputtering rates. The sputtering rates increase for the higher F/Al concentration ratios.

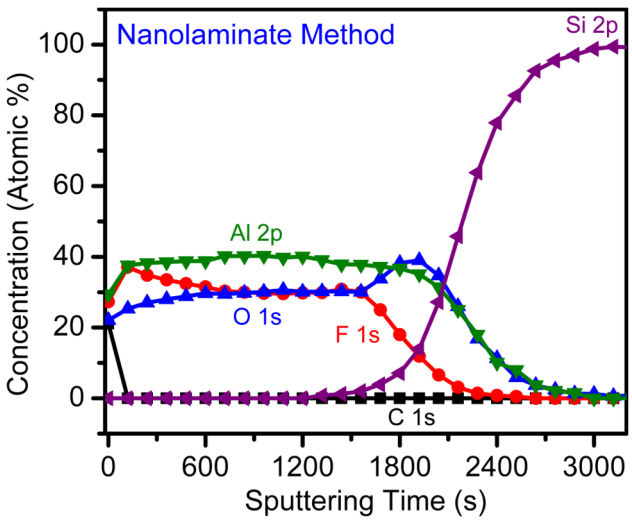

FIG. 11. Compositional depth profile of AlO_xF_y thin films with a thickness of 30 nm grown by the 5:1 nanolaminate method on the Si(111) substrate at 150 °C measured by x-ray photoelectron spectroscopy (XPS).

Sputtering rates can be roughly correlated with thermodynamic data. Physical sputtering rates are typically assumed to be related to the sublimation enthalpy,[44–46] heat of formation,[47,48] and boiling temperature.[42] The sublimation enthalpies of Al_2O_3 and AlF_3 are 643 and 286 kJ/mol, respectively.[49,50] The heats of formation of Al_2O_3 and AlF_3 are −1669.8 and −1507.8 kJ/mol,

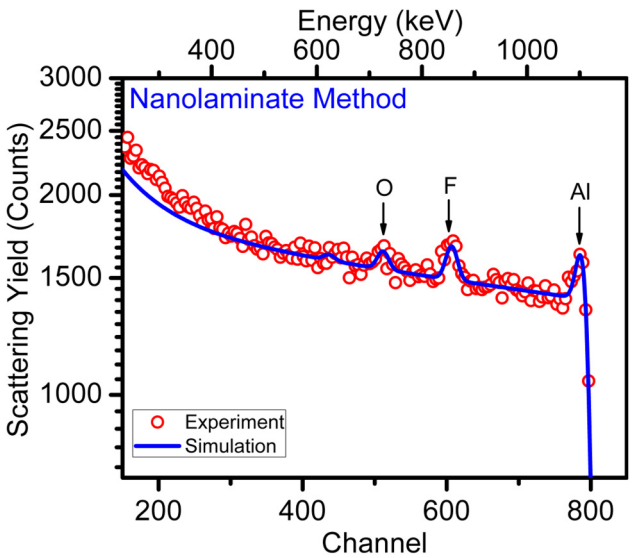

FIG. 12. Rutherford backscattering spectrum (RBS) of AlO_xF_y thin films with a thickness of 30 nm grown by the 5:1 nanolaminate method on the Si(111) substrate at 150 °C.

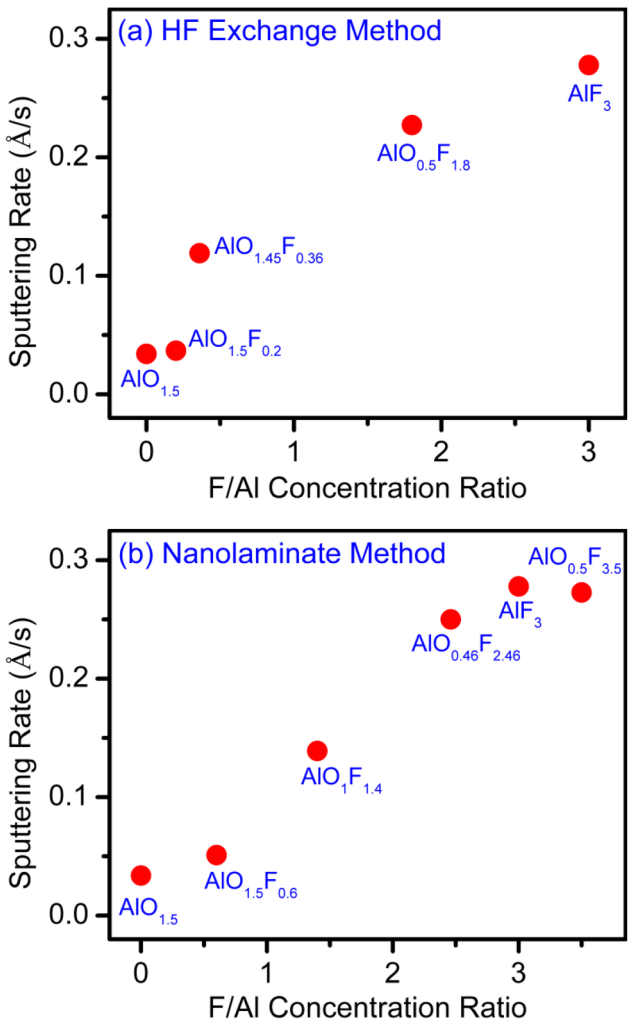

FIG. 13. Sputtering rate vs F/Al concentration ratio for AlO_xF_y thin films grown by (a) the HF exchange method and (b) the nanolaminate method.

respectively. Likewise, the boiling temperatures of Al_2O_3 and AlF_3 are 2977 and 1290 °C, respectively. Another factor may be the bonding in Al_2O_3 and AlF_3 and the resulting leaving groups during sputtering. AlF_3 is a molecule and has strong F bridge-bonding in the AlF_3 molecular solid. The leaving groups during AlF_3 sputtering may be AlF_3 molecules. In contrast, Al_2O_3 has strong Al–O ionic bonds and no preferred molecular complex that can leave during sputtering. Based on all of these factors, Al_2O_3 may be expected to be more resistive to physical sputtering than AlF_3.

The corrosion properties of these coatings will depend both on physical sputtering and on chemical sputtering. Chemical sputtering depends on the chemical reaction on the surface in the presence of plasma ions and the plasma environment.[51] There can be synergistic effects where the plasma etch rate is much higher in the presence of both plasma ions and chemical species on the surface.[52] Both Al_2O_3 and AlF_3 show high resistance to chemical sputtering in oxygen-rich and fluorine-rich plasma environments, respectively. Consequently, the corrosion resistance of the AlO_xF_y films can be tailored with precise control over the AlO_xF_y stoichiometry to obtain the optimum performance.

IV. CONCLUSIONS

Aluminum oxyfluoride (AlO_xF_y) thin films were grown using ALD techniques at 150 °C with TMA, H_2O, and HF as the reactants. The AlO_xF_y films were deposited using two pathways based on the HF exchange method and the nanolaminate method. The AlO_xF_y growth was investigated using *in situ* QCM studies. Both the HF exchange method and the nanolaminate method displayed linear growth. AlO_xF_y films with variable stoichiometry could be deposited by varying the conditions during the HF exchange method and the nanolaminate method.

Growth by the HF exchange method is based on the thermodynamically favorable HF reaction with Al_2O_3. Fluorine is incorporated into the Al_2O_3 layer by an O to F exchange. Based on the QCM mass changes, the HF exchange reaction was dependent on HF pressure. The stoichiometry of the AlO_xF_y films was determined by the HF pressure and the thickness of the underlying Al_2O_3 layer prior to HF exposure.

The growth of AlO_xF_y films by the nanolaminate method is based on the sequential deposition of a number of cycles for Al_2O_3 ALD and then a number of cycles for AlF_3 ALD. AlF_3 ALD growth on the Al_2O_3 layer displayed evidence of a significant O to F exchange during the first HF exposure. In contrast, Al_2O_3 ALD growth on the AlF_3 layer displayed only slight evidence of an F to O exchange during the first H_2O exposure. This difference in exchange is expected based on the thermochemistry of fluorination of Al_2O_3. The stoichiometry of the AlO_xF_y films was dependent on the ratio of the number of Al_2O_3 ALD cycles and the number of AlF_3 ALD cycles during AlO_xF_y growth.

XPS depth-profile studies revealed a uniform distribution of Al, O, and F in all the AlO_xF_y thin films deposited with the HF exchange method and the nanolaminate method. The stoichiometry of the various AlO_xF_y films was also determined using RBS measurements. The stoichiometry could be continuously varied from Al_2O_3 to AlF_3 by changing the reaction conditions. The physical sputtering rates were also measured during the XPS depth-profile measurements. The lowest sputtering rate was 0.03 Å/s for the Al_2O_3 films. The highest sputtering rate was 0.28 Å/s for AlF_3 films. All AlO_xF_y thin films showed higher sputtering rates with increasing F/Al concentration ratios.

ACKNOWLEDGMENT

The authors thank Ryan Thorpe in the Laboratory for Surface Modification at Rutgers University for the RBS measurements.

REFERENCES

[1]V. M. Donnelly and A. Kornblit, J. Vac. Sci. Technol. A **31**, 050825 (2013).
[2]D. B. Graves, IEEE Trans. Plasma Sci. **22**, 31 (1994).
[3]M. A. Lieberman and A. J. Lichtenberg, *Principles of Plasma Discharges and Materials Processing*, 2nd ed. (Wiley, New York, 2005).

[4]K. Miwa, N. Takada, and K. Sasaki, J. Vac. Sci. Technol. A **27**, 831 (2009).
[5]A. Agarwal and M. J. Kushner, J. Vac. Sci. Technol. A **26**, 498 (2008).
[6]M. J. Sowa, J. Vac. Sci. Technol. A **32**, 01a106 (2014).
[7]S. L. Xu, Z. W. Sun, X. Y. Qian, J. Holland, and D. Podlesnik, J. Vac. Sci. Technol. B **19**, 166 (2001).
[8]T. Ma, T. List, and V. M. Donnelly, J. Vac. Sci. Technol. A **35**, 031303 (2017).
[9]Y. Shiba, A. Teramoto, T. Goto, Y. Kishi, Y. Shirai, and S. Sugawa, J. Vac. Sci. Technol. A **35**, 021405 (2017).
[10]Y.-C. Cao, L. Zhao, J. Luo, K. Wang, B.-P. Zhang, H. Yokota, Y. Ito, and J.-F. Li, Appl. Surf. Sci. **366**, 304 (2016).
[11]D. M. Kim, Y. S. Oh, S. Kim, H. T. Kim, D. S. Lim, and S. M. Lee, Thin Solid Films **519**, 6698 (2011).
[12]T.-K. Lin, W.-K. Wang, S.-Y. Huang, C.-T. Tasi, and D.-S. Wuu, Nanomaterials **7**, 183 (2017).
[13]K. Miyashita, T. Tsunoura, K. Yoshida, T. Yano, and Y. Kishi, Jpn. J. Appl. Phys. **58**, SEEC01 (2019).
[14]R. Tahara, T. Tsunoura, K. Yoshida, T. Yano, and Y. Kishi, Jpn. J. Appl. Phys. **57**, 06jf04 (2018).
[15]T. Tsunoura, K. Yoshida, T. Yano, and Y. Kishi, Jpn. J. Appl. Phys. **56**, 06hc02 (2017).
[16]K. V. Dukel'skii and S. K. Evstrop'ev, J. Opt. Technol. **78**, 137 (2011).
[17]M. Kitano, M. Nagase, Y. Shirai, and T. Ohmi, "Al_2O_3 passivation film on austenitic stainless steel free from plasma damage," in *Corrosion and Corrosion Protection*, edited by J. D. Sinclair, R. P. Frankenthal, E. Kalman, and W. Plieth (Electrochemical Society, Pennington, NJ, 2001), Vol. 2001/22, p. 115.
[18]S. Fujihara, T. Kato, and T. Kimura, J. Mater. Sci. Lett. **20**, 687 (2001).
[19]S. J. Jiang, Z. C. Jin, and C. G. Granqvist, Appl. Opt. **27**, 2847 (1988).
[20]D. S. Kim, Y. Y. Yu, and K. Char, J. Appl. Phys. **96**, 2278 (2004).
[21]W.-K. Wang, Y.-X. Lin, and Y.-J. Xu, Nanomaterials **8**, 936 (2018).
[22]S. Y. Zheng, A. M. Andersson-Fäldt, B. Stjerna, and C. G. Granqvist, Appl. Opt. **32**, 6303 (1993).
[23]T.-K. Lin, D.-S. Wuu, S.-Y. Huang, and W.-K. Wang, Coatings **8**, 373 (2018).
[24]G. Malandrino, L. M. S. Perdicaro, and I. L. Fragalà, Chem. Vap. Depos. **12**, 736 (2006).
[25]V. Cremers, R. L. Puurunen, and J. Dendooven, Appl. Phys. Rev. **6**, 021302 (2019).
[26]J. W. Elam, D. Routkevitch, P. P. Mardilovich, and S. M. George, Chem. Mater. **15**, 3507 (2003).
[27]S. M. George, Chem. Rev. **110**, 111 (2010).
[28]V. Miikkulainen, M. Leskela, M. Ritala, and R. L. Puurunen, J. Appl. Phys. **113**, 021301 (2013).
[29]R. L. Puurunen, J. Appl. Phys. **97**, 121301 (2005).
[30]A. Rahtu, T. Alaranta, and M. Ritala, Langmuir **17**, 6506 (2001).
[31]M. D. Groner, J. W. Elam, F. H. Fabreguette, and S. M. George, Thin Solid Films **413**, 186 (2002).
[32]M. D. Groner, F. H. Fabreguette, J. W. Elam, and S. M. George, Chem. Mater. **16**, 639 (2004).
[33]R. A. Wind and S. M. George, J. Phys. Chem. A **114**, 1281 (2010).
[34]A. C. Dillon, A. W. Ott, J. D. Way, and S. M. George, Surf. Sci. **322**, 230 (1995).
[35]A. W. Ott, J. W. Klaus, J. M. Johnson, and S. M. George, Thin Solid Films **292**, 135 (1997).
[36]J. W. Elam, M. D. Groner, and S. M. George, Rev. Sci. Instrum. **73**, 2981 (2002).
[37]Y. Lee, J. W. DuMont, A. S. Cavanagh, and S. M. George, J. Phys. Chem. C **119**, 14185 (2015).
[38]Y. Lee, H. X. Sun, M. J. Young, and S. M. George, Chem. Mater. **28**, 2022 (2016).
[39]*HSC Chemistry*; HSC Chemistry 5.1, Outokumpu Research Oy, Pori.
[40]J. D. Targove, B. G. Bovard, L. J. Lingg, and H. Angus Macleod, Thin Solid Films **159**, L57 (1988).
[41]A. M. Cano, A. E. Marquardt, J. W. DuMont, and S. M. George, J. Phys. Chem. C **123**, 10346 (2019).
[42]D.-M. Kim, M.-R. Jang, Y.-S. Oh, S. Kim, S.-M. Lee, and S.-H. Lee, Surf. Coat. Technol. **309**, 694 (2017).
[43]M. P. Seah and T. S. Nunney, J. Phys. D: Appl. Phys. **43**, 253001 (2010).
[44]B. J. Garrison, Nucl. Instrum. Methods Phys. Res. B **40/41**, 313 (1989).
[45]P. Sigmund, Phys. Rev. **184**, 383 (1969).
[46]M. W. Thompson, Vacuum **66**, 99 (2002).
[47]D.-H. Kim, G.-H. Lee, S. Yup Lee, and D. Hyun Kim, J. Cryst. Growth **286**, 71 (2006).
[48]S. V. Baryshev and E. Thimsen, Chem. Mater. **27**, 2294 (2015).
[49]B. Brunetti, V. Piacente, and P. Scardala, J. Chem. Eng. Data **54**, 940 (2009).
[50]J. M. Lihrmann, J. Eur. Ceram. Soc. **28**, 649 (2008).
[51]Y.-Y. Tu, T. J. Chuang, and H. F. Winters, Phys. Rev. B **23**, 823 (1981).
[52]J. W. Coburn and H. F. Winters, J. Appl. Phys. **50**, 3189 (1979).